SPECIAL
International Symposium on Tropospheric Profiling
COLLECTION

# In Situ Samplings and Remote Sensing Measurements to Characterize Aerosol Properties over Southeast Italy

V. BELLANTONE, I. CAROFALO, F. DE TOMASI, M. R. PERRONE, M. SANTESE, A. M. TAFURO, AND
A. TURNONE

*Physics Department, University of Salento, Lecce, Italy*

## ABSTRACT

Ground-based particulate matter (PM) samplers, an XeF Raman lidar operating in the framework of the European Aerosol Research Lidar Network (EARLINET), and a sun/sky radiometer operating in the framework of the Aerosol Robotic Network (AERONET) have been used to characterize vertical profiles, optical and microphysical properties, and chemical composition of aerosols during the 29 June–1 July 2005 dust outbreak that occurred over the central-eastern Mediterranean. Aerosol backscatter coefficient, total depolarization, and lidar ratio vertical profiles revealed that a well-mixed dust layer extending from ~0.5 to 6 km was present over southeastern Italy on 30 June. Sun/sky radiometer measurements revealed a bimodal lognormal size distribution during all measurement days. The particle volume distribution was found to be well correlated either to the PM mass distribution measured at ground by a seven-stage cascade impactor and to the fine to total suspended PM mass ratio measured by ground-based PM samplers. Scanning electron microscopy and ion chromatography analyses on PM samples revealed that coarse-mode aerosols were mainly made of carbonate, aluminum-silicate, and sea salt particles. Carbon, sulfate, and nitrate particles were the main components of fine-mode aerosols representing more than 50% of the total aerosol load; the significant role of fine-mode anthropogenic particles during a dust event is highlighted.

Finally, the potential capabilities of complementary measurements by passive and active remote sensing techniques and in situ observations to retrieve the vertical distribution of the particle number and mass concentration are analyzed and discussed.

## 1. Introduction

The importance of a quantitative and qualitative assessment of atmospheric aerosol characteristics has been recognized for many years, since aerosols are responsible for direct and indirect effects on atmospheric processes and hence on climate (e.g., Schwartz and Andreae 1996). Human health is also expected to be quite affected by the aerosol fine fraction. The variety of sources and chemical processes that contribute to the aerosol creation and their relatively short lifetime make the aerosol properties extremely variable both on temporal and spatial scales. Thus, the question of what kind and which quantities of aerosols are present in a region can only be answered in a statistical sense. Regular

measurements can define background conditions, but detailed studies of specific events are also important. Because of the complexity of aerosols, a single measurement technique delivering all the relevant information is not available: thus, a multi-instrument approach is needed. In situ measurements at ground level are the most important for the air quality characterization. These measurements can in principle give complete information because mass, size distribution, chemical composition, and morphology can all be experimentally determined. However, this information is insufficient for the characterization of aerosol interactions with the solar radiation because aerosols in the atmosphere participate to this process (e.g., Tegen et al. 1997). Remote sensing tools, such as lidars and radiometers, are generally used to characterize the aerosol load above ground level. Furthermore, it is very important to perform these measurements in a global way, to cover wide regions and possibly the whole world. This can only be done by networks of instruments such as the European

*Corresponding author address:* Maria Rita Perrone, Physics Department, University of Salento, Via per Arnesano, 73100 Lecce, Italy.
E-mail: perrone@le.infn.it

Aerosol Research Lidar Network (EARLINET; Matthias et al. 2004a) and the Aerosol Robotic Network (AERONET; Holben et al. 1998) or satellite-based instruments (Kaufman et al. 2002). Remote sensing measurements can allow only the retrieval of optical and microphysical aerosol properties. Thus, it becomes evident that a complete characterization of aerosols needs the use of different and complementary instruments. Data from ground-based lidar and sun photometer, and particle counters on board an instrumented ultralight aircraft, have been used by Di Iorio et al. (2003) to characterize aerosol properties at the island of Lampedusa, during the Photochemical Activity and Ultraviolet Radiation II campaign. Combined observations with an advanced aerosol water vapor temperature Raman lidar and a sun photometer have been used by Müller et al. (2003) for a detailed characterization of geometrical and optical properties of a continental-scale Saharan dust event observed over Leipzig, Germany. The complementary use of three-dimensional chemical transport models and satellite observations has been illustrated by Robles Gonzalez et al. (2003) to show that models can provide information on the temporal and spatial (vertical and horizontal) distributions as well as chemical composition of the different types of aerosol. Different airborne and ground-based aerosol measurements of a forest fire haze layer over a site in northeastern Greece have instead been used by Formenti et al. (2002) for closure tests and the radiative transfer calculations of the spectral shortwave, downwelling irradiance at the surface.

Regular measurements by ground-based particulate matter samplers (Buccolieri et al. 2006) and active (lidar) and passive (sun/sky radiometer) remote sensing techniques (De Tomasi and Perrone 2003; Perrone et al. 2005) are performed at the Physics Department of Salento's University (40.33°N, 18.12°E) to properly characterize aerosol properties and infer aerosol effects on air quality and climate. The use of complementary measurements to characterize optical and microphysical properties, and the chemical composition of aerosols during the 29 June–1 July 2005 dust outbreak that occurred over the central-eastern Mediterranean, is illustrated in this paper. The main goal of the paper is to demonstrate the potential capabilities of complementary measurements to retrieve the vertical distribution of the particle number and mass concentration.

The Physics Department of Salento's University is located in the suburb of Lecce, Italy, in the middle of a narrow peninsula (~35 km from coast to coast), which is ~900 km away from the African coast, with no major localized sources of aerosols. As a consequence, this site is well suited for the studies of dust outbreaks from the Sahara. Previous studies revealed that Saharan dust intrusions considerably modify both the background level of aerosol mass and the aerosol composition (Blanco et al. 2003; De Tomasi et al. 2003). Therefore, these events require a proper combination of complementary measurements by passive and active remote sensing techniques and in situ observations to retrieve vertical distribution, concentration, elemental composition, dimension, and optical properties of aerosol particles. The instruments used in this study and described in the next section, are a combined elastic–Raman lidar, a multiwavelength sun/sky radiometer, particle samplers, and a multistage cascade impactor. Aerosol particles collected at the ground by the last two instruments are further analyzed by scanning electron microscopy and ion chromatography to characterize their morphology, and their elemental and chemical composition. Another piece of information, which is important to properly characterize the aerosols, is the history of air masses over the observation site: this allows us to identify major nonlocal aerosol sources and, hence, infer transformations of aerosols during the transport. To this end, analytical back trajectories and satellite images are used for the case study of this paper.

## 2. Experimental facilities

Particulate matter (PM) measurements are regularly performed at ~15 m above ground level at the Physic Department of Salento's University since 2004 by different devices. A low flow (2.3 $m^3 h^{-1}$) FH 95 KF (ESM Andersen) particulate sampler equipped with PM10 (or PM2.5) inlet, is used to collect atmospheric particles on 47-mm-diameter cellulose nitrate filters having a nominal pore size of 0.8 $\mu$m. Particulate matter concentrations are determined by the gravimetric method. The filters are then used for elemental and chemical analyses. The FH 62 I-R (ESM Andersen) sampler, which is a radiometric instrument, is instead used for the continuous mass determination of the total suspended particulate (TSP) matter collected on a quartz filter tape. The FH 62 I-R sampler is equipped with a Kr-85 $\beta$ source for the determination of the ambient mass concentration by the $\beta$ radiation absorption technique (e.g., Klein et al. 1984). Fractional collection of aerosol particles is performed by an OH-610-C (Kalman System) seven-stage cascade impactor that operating at a flow rate of 1.5 $m^3 h^{-1}$, allows fractional collection of particles on seven quartz filters with 50% effective-cut diameter ($d_c$) of 5.7, 2.7, 1.4, 0.65, 0.35, 0.14, and 0.08 $\mu$m, respectively.

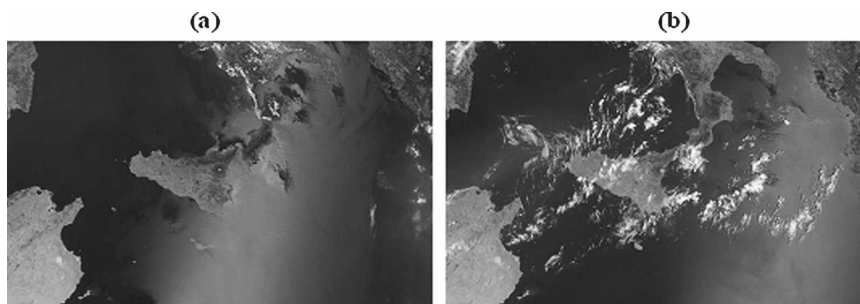Morphological, elemental, and chemical analyses by scanning electron microscopy (SEM) and ion chroma-

FIG. 1. MODIS images of the Mediterranean by the *Terra* satellite at (a) 0955 UTC 29 Jun 2005 (see online at http://rapidfire.sci.gsfc.nasa.gov/aeronet/?ETNA/2005180/ AERONET_ETNA.2005180.terra) and (b) at 0945 UTC 1 Jul 2005 (see online at http:// rapidfire.sci.gsfc.nasa.gov/aeronet/?ETNA/2005182/AERONET_ETNA.2005182.terra). The light gray area over the Mediterranean Sea is due to the presence of dust particles.

tography are performed to characterize the particles collected on filters.

Ground meteorological parameters (e.g., temperature, relative humidity, wind direction, and wind speed) and the height of the planetary boundary layer (PBL) are also continuously monitored. PBL heights are retrieved by sonic detection and ranging (SODAR; Remtech PA1) measurements.

The lidar observations employed in this study have been performed in the framework of the European Project EARLINET (Matthias et al. 2004a) by a Raman lidar operating at 351 nm. The Raman lidar has been designed to derive vertical profiles of aerosol extinction and backscatter coefficients, lidar ratios, and total depolarization ratios during nighttime operations; and to get aerosol backscatter coefficient and total depolarization ratio vertical profiles during daytime measurements. Details on experimental apparatus and data analysis are reported in De Tomasi and Perrone (2003) and De Tomasi et al. (2006). We remind readers that the lidar system is based on a XeF excimer laser (351 nm) and that the backscattered radiation is monitored in two different spectral channels: elastic and Raman $N_2$, at 351 nm and 384 nm, respectively. The lidar system overlap function is estimated to be equal to 1 between 350 and 500 m (Matthias et al. 2004b).

An AERONET sun/sky radiometer is used to retrieve columnar aerosol volume size distributions, real and imaginary refractive indices ($n$ and $k$), single-scattering albedo (SSA) values, and aerosol optical thicknesses (AOTs). The automatic, robotically operated sun-tracking sky radiometer, with a 1.2° field of view and two detectors, measures the direct sun radiance at eight spectral channels: 340, 380, 440, 500, 670, 870, 940, and 1020 nm, while measurements of sky radiance are made at 440, 670, 870, and 1020 nm. Holben et al. (1998, 2001) give detailed descriptions of the in-

strument and data acquisition procedures. A flexible inversion algorithm, developed by Dubovik and King (2000), is used to retrieve columnar aerosol parameters from direct-sun and diffuse-sky radiance measurements. A brief discussion on the accuracy of individual retrievals is reported in Dubovik et al. (2002). Cloud-screened (level 1.5) aerosol products (Smirnov et al. 2000) from the spheroid almucantar retrieval model (Dubovik et al. 2006) are used in this study.

## 3. Methods and measurements

True color images by the Moderate Resolution Imaging Spectroradiometer (MODIS; available online at http://modis.gsfc.nasa.gov/) and three-dimensional, 7-day analytical back trajectories by the National Aeronautics and Space Administration (NASA) Goddard Space Flight Center (GSFC; available online at http:// aeronet.gsfc.nasa.gov/) are used to infer the presence of a dust outbreak over southeastern Italy from 29 June to 1 July 2005. The MODIS image at 0955 UTC from the *Terra* satellite (Fig. 1a) reveals that a dust plume (light gray area) extends over the central-eastern Mediterranean on 29 June. According to the MODIS image of Fig. 1b, provided by the *Terra* satellite at 0945 UTC, a dust plume was also present over the central-eastern Mediterranean on 1 July. The 7-day analytical back trajectories are provided by NASA for each AERONET site, at eight distinct arrival pressure levels (950, 850, 700, 500, 400, 300, 250, and 200 hPa) and at two arrival times (0000 and 1200 UTC). The trajectories are based on a kinetic trajectory analysis using NASA Global Modeling and Assimilation Office (GMAO) assimilated gridded data. Figure 2a shows the pathways of the 950-, 850-, 700-, and 500-hPa back trajectories that reach the monitoring site on 30 June at 1200 UTC. The pressure level of each back trajectory as a function of
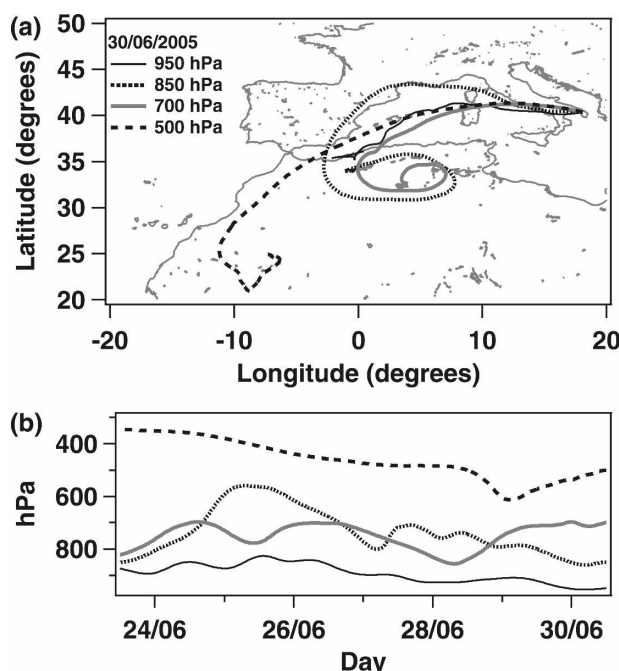
FIG. 2. (a) The 7-day analytical back trajectories for the air masses reaching Lecce at 1200 UTC 30 Jun 2005. (b) The pressure level of each back trajectory as a function of time.
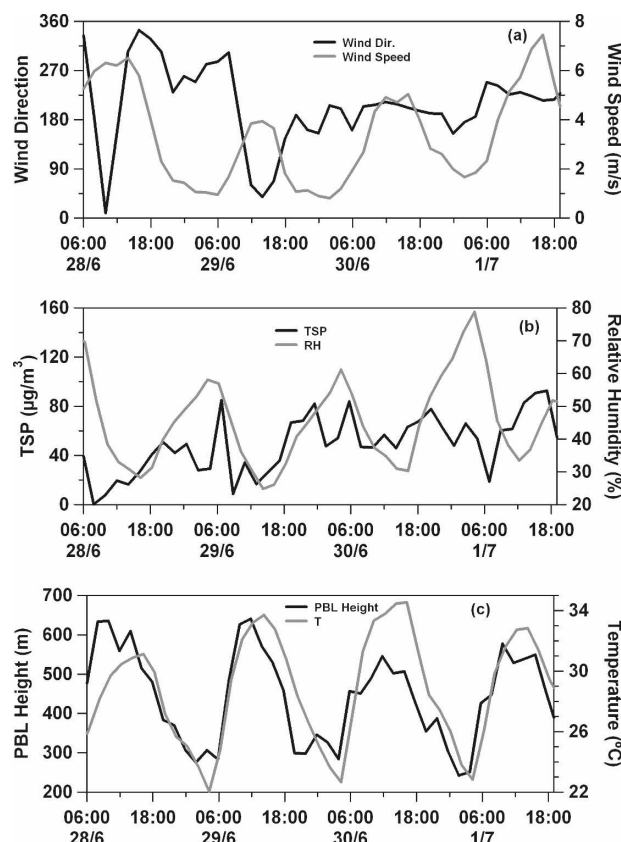


FIG. 3. (a) Temporal evolution of wind speed (gray line) and wind direction (black line) at ground. (b) Temporal evolution of the TSP mass concentration (black line) and of the ground relative humidity (gray line). (c) Evolution of PBL height (black line) and ground temperature (gray line). All figures refer to 28 Jun–1 Jul 2005.

time is shown in Fig. 2b. We observe from Fig. 2 that all back trajectories traveled over northwestern Africa before reaching the monitoring site and that the initial pressure level of the 950-, 850-, and 700-hPa back trajectories was larger than 800 hPa.

### a. Ground meteorological parameters and mass concentrations by PM samplers and a seven-stage cascade impactor

Ground measurements of meteorological parameters, PBL heights, and PM mass concentrations are reported and analyzed in this section to infer main effects of African dust outbreaks on ground atmospheric parameters. Figure 3a shows the temporal evolution of wind speed (gray line) and direction (black line) from 28 June to 1 July 2005. The temporal evolution of the TSP mass concentration provided by the FH 62 I-R sampler (black line) and of the ground relative humidity (gray line) is plotted in Fig. 3b. Temperature (gray line) and PBL height (black line) evolutions are in Fig. 3c. We observe from Fig. 3a (black line) a significant change of wind direction on 29 June: winds from the south blow over the monitoring site from the night of 29 June at least until the night of 1 July. The wind speed is higher than 4 m s$^{-1}$ on 30 June at midday. In addition, Fig. 3 reveals that temperature peak values are largest (Fig. 3a, gray line) and that relative humidity peak val-

ues are smallest (Fig. 3b, gray line) on 29 and 30 June. The latter results may indicate that warm air masses from northwestern Africa have been advected over the monitoring site on those days, in accordance to back trajectories (Fig. 2).

As it is well known, the temporal evolution of the ground PM concentration is generally anticorrelated to that of the PBL height (Allegrini et al. 1994): higher PM concentrations are found at night when the PBL height is lower, while the PM concentration reaches minimum values during the daytime hours as a consequence of the diurnal increase of the PBL height. Accordingly, the comparison of Fig. 3b (black line) and Fig. 3c (black line) shows that the TSP mass concentration has minimum values at about 0900 UTC on 28 and 29 June. However, as a consequence of the advection of warm air masses from northwestern Africa, the daily cycle of the mass concentration is not observed on 30 June: TSP mass concentrations are rather high during the whole day. The smaller difference between night
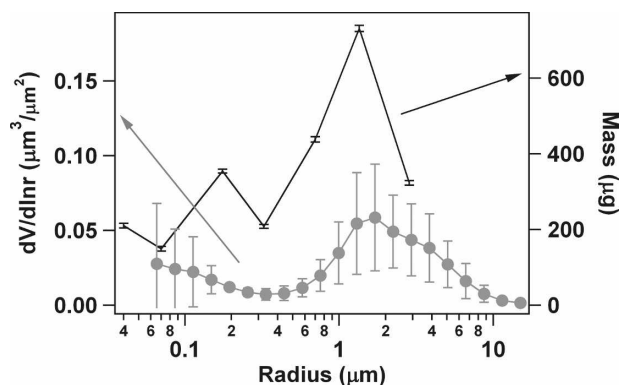
FIG. 4. Particle mass vs the 50% effective-cut radius of the seven-stage cascade impactor filters (black symbols) and mean columnar volume size distribution (gray symbols) calculated by averaging 11 profiles retrieved on 30 Jun and 1 Jul by sun/sky radiometer measurements performed during the 48-h impactor's measurement time. Vertical error bars represent ±1 standard deviation of the average values.

and day PBL heights on 30 June is a contributing factor. It is also worth noting that the TSP mass concentration gets minimum values on 1 July at about 0800 UTC.

The 24-h measurements of PM10 and PM2.5 particles, respectively, by the FH 95 sampler revealed that the daily-average PM10 mass concentration was $46 \pm 1$ $\mu$g m$^{-3}$ on 29 June and that the daily-average PM2.5 mass concentration was $33 \pm 1$ $\mu$g m$^{-3}$ on 30 June. From the TSP matter plot of Fig. 3b, we have calculated the mean TSP mass concentration during the 24-h measurement time of PM10 and PM2.5 particles: $52 \pm 2$ $\mu$g m$^{-3}$ on 29 June and $55 \pm 3$ $\mu$g m$^{-3}$ on 30 June. Hence, 88% of the TSP matter was made of PM10 particles on 29 June, while 60% of the TSP matter was made of PM2.5 particles on 30 June. The latter data show the significant contribution of fine-mode particles during both measurement days, despite the dust event.

The 48-h fractional measurements of particles by the seven-stage cascade impactor have been performed from 0730 UTC 30 June to 0730 UTC 2 July. The particle mass plot as a function of the 50% effective-cut radius ($r_c$) of the impactor filters is shown in Fig. 4 (black symbols). Uncertainties on mass values are lower than 5%. Figure 4 (black symbols) reveals that the particle mass reaches higher values on the filters with 1.85- and 0.175-$\mu$m $r_c$ values. In addition, we mention that the mass collected on the filters with $r_c$ values smaller than 1.67 $\mu$m is 51% of the total particle mass collected on the seven filters in satisfactory accordance with the PM2.5/TSP mass ratio (60%) retrieved by the PM2.5 and the TSP measurements performed on 30 June.
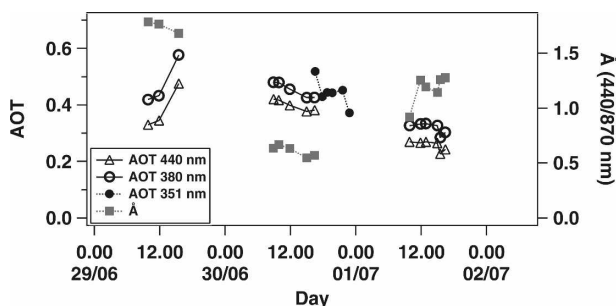


FIG. 5. Evolution of the AOT at 380 (open dots) and at 440 nm (open triangles) and of the Ångstrom coefficient at 440/870 nm (gray full boxes) from 29 Jun to 2 Jul 2005 by sun/sky radiometer measurements. The evolution of the AOT at 351 nm (full dots) retrieved on 30 Jun 2005 by lidar measurements is also reported.

## b. Aerosol properties by sun/sky radiometer measurements

Sun/sky radiometer measurements provide columnar values of the microphysical properties of aerosol particles and represent an important tool to follow the temporal evolution of pollution events during the daytime hours (Tafuro et al. 2006). The AOT is the most commonly used parameters in aerosol studies. Figure 5 shows the evolution of the AOT at 380 (open dots) and at 440 nm (open triangles) from 29 June to 2 July. The AOT accuracy is ±0.01 or slightly higher in the 440–1020-nm range and about 0.015–0.02 in the UV (Holben et al. 1998; Eck et al. 1999). The temporal evolution of the Ångström exponent (computed from AOT values at 440 and 870 nm) is also reported in Fig. 5 (gray symbols). The Ångström uncertainties are smaller than 5%. The Ångström exponent mainly depends on the aerosol size distribution: typical values range from Å > 2.0 for fresh smoke particles, which are dominated by accumulation mode aerosols, to nearly zero for large dust particles (Dubovik et al. 2000). Hence, for its high sensitivity to the aerosol particle size, Å is a good marker to trace the temporal evolution of particle size distribution changes during pollution events. AOTs and Ångström exponents are generally anticorrelated during dust outbreaks (Tafuro et al. 2006). Accordingly, Fig. 5 shows that AOT increases on 29 June as a consequence of the advection of air masses from Sahara (Fig. 1a), while Ångström values appear to slightly decrease with time for the contribution of large dust particles. We also observe that Ångström values that are ~1.8 on 29 June, reduce to about 0.6 on 30 June, and increase to ~1.3 on 1 July. Latter results may indicate that the contribution of large dust particles over the monitoring site was more significant on 30 June. The time evolution of temperature, relative humidity, and TSP matter also support the last conclusion. Rather
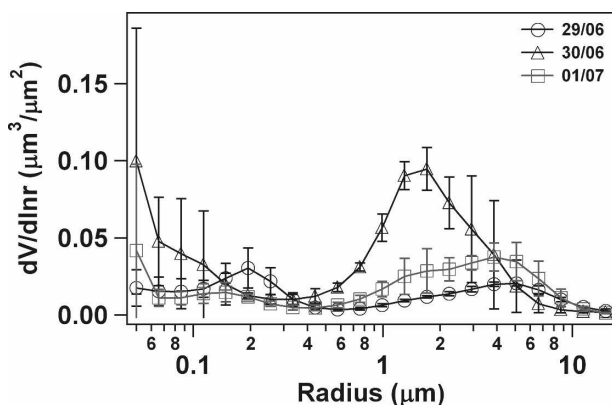
FIG. 6. Mean columnar volume size distribution of 29 Jun (open dots), 30 Jun (open triangles), and 1 Jul 2005 (open boxes) retrieved from sun/sky radiometer measurements. Vertical error bars represent ±1 standard deviation of the average values.

TABLE 1. Daily average values at 440 nm and corresponding standard deviations of the real ($n$) and imaginary ($k$) refractive index and of the SSA retrieved from sun/sky radiometer measurements.

| Date | $n$ | $k$ | SSA |
|---|---|---|---|
| 29 Jun 2005 | $1.57 \pm 0.04$ | $0.010 \pm 0.002$ | $0.93 \pm 0.01$ |
| 30 Jun 2005 | $1.5 \pm 0.1$ | $0.006 \pm 0.003$ | $0.90 \pm 0.03$ |
| 1 Jul 2005 | $1.58 \pm 0.04$ | $0.005 \pm 0.004$ | $0.94 \pm 0.05$ |

high TSP mass concentrations have been monitored all day on 30 June (Fig. 3), but the TSP mass concentration again gets minimum values on the early morning of 1 July. The Ångström value changes are mainly related to changes of the atmospheric particle size distribution, while AOT temporal evolutions provide valuable data on the evolution of pollution event intensities. Figure 5 shows that the AOT at 380 nm increases with the daytime hours up to 0.6 on 29 June, decreases during 30 June, and reduces to ~0.3 on 1 July.

Figure 6 shows the mean columnar volume size distribution retrieved (spheroid almucantar retrieval model) from AERONET sun/sky radiometer measurements performed on 29 June (open dots), 30 June (open triangles), and 1 July (open boxes) at different daytime hours. In particular, the profiles of 29 June, 30 June, and 1 July have been calculated by averaging three, four, and six different volume size distribution profiles, respectively. Vertical error bars in Fig. 6 represent ±1 standard deviation of the average value and reveal the daily variability of the size distribution. Analyses by Dubovik et al. (2000, 2002) have shown that $dV(r)/d\ln r$ values are retrieved with accuracy levels of the order of 15%–35% for $0.1\ \mu m \leq r \leq 7\ \mu m$. Figure 6 reveals that the columnar volume size distribution of the aerosol particles can be considered at least bimodal during all measurement days: minimum values are reached at $r \cong 0.4\ \mu m$ on 29 June and 1 July, and at $r \cong 0.3\ \mu m$ on 30 June. According to the Ångström coefficient temporal evolution, Fig. 6 (open triangles) shows that the contribution of coarse-mode particles is significantly larger on 30 June.

The mean columnar volume size distribution calcu-

lated by averaging the 11 profiles retrieved by the sun/sky radiometer measurements performed from 0730 UTC 30 June to 0730 UTC 1 July (corresponding to the 48-h measurement time of the cascade impactor), is plotted in Fig. 4 (gray symbols). Vertical error bars represent ±1 standard deviation of the average value and reveal the size distribution variability. The comparison of Fig. 4 and Fig. 6 reveals that the mean columnar volume size distribution of Fig. 4 is quite affected by the columnar volume size distribution retrieved on 30 June. We observe from Fig. 4 that the coarse-mode volume size distribution is peaked at $r$ ~1.5 $\mu m$, in accordance to the mass distribution plot (black symbol) retrieved by the seven-stage cascade impactor measurements. In addition, both cascade impactor mass distribution and volume size distribution reach a minimum at $r \sim 0.3\ \mu m$. The latter results reveal a good correlation between the 48-h-averaged particle mass distribution at ground and the mean columnar volume size distribution retrieved from sun/sky radiometer measurements performed within the same time interval. We believe that latter results may indicate that ground-sampled particles are representative of aerosol particles above ground level. Lidar measurements that will be presented and analyzed in the next section support the last comment.

Daily mean values at 440 nm and corresponding standard deviations of the real ($n$) and imaginary ($k$) refractive index, and of the SSA are given in Table 1. According to Dubovik et al. (2000, 2002), the expected accuracy for the real part of the refractive index is within the 0.025–0.04 range for AOTs (440 nm) >0.2. In contrast, $k$ values are retrieved with errors of the order of 50% for AOTs (440 nm) >0.2. Uncertainties on SSA values are of 0.03 for AOTs (440 nm) >0.2. Table 2 reveals that $n$, $k$, and SSA standard deviations are close to corresponding retrieval uncertainties. Nevertheless, it is worth noting that the data of 30 June are rather close to the average values of $n$, $k$, and SSA that have recently been reported by some of the authors to characterize dust particles over the central-eastern Mediterranean Basin under medium–high dust loads (Tafuro et al. 2006).

TABLE 2. Weight percentage of selected elements in the analyzed impactor filters. Here $d_c$ represents the 50% effective-cut diameter ($\mu$m) of the seven impactor filters.

| $d_c$ ($\mu$m) | C | N | F | Na | Mg | Al | P | S | Cl | K | Ca | Ti | V | Mn | Fe | Cu | Zn |
|---|---|---|---|---|---|---|---|---|---|---|---|---|---|---|---|---|---|
| 5.70 | 31.0 | 0.6 | 0.1 | 5.8 | 5.4 | 13.3 | 0.3 | 1.2 | 4.7 | 4.4 | 28.6 | 0.1 | 0 | 0 | 4.1 | 0 | 0 |
| 2.70 | 29.2 | 0.7 | 0 | 7.3 | 5.1 | 13.9 | 0.1 | 1.2 | 3.7 | 3.5 | 30.1 | 0.2 | 0 | 0 | 4.9 | 0 | 0 |
| 1.40 | 28.9 | 3.8 | 0 | 8.5 | 5.0 | 13.6 | 0.2 | 3.5 | 4.6 | 3.2 | 23.8 | 0 | 0 | 0 | 4.8 | 0 | 0 |
| 0.65 | 36.8 | 0.9 | 0.8 | 5.1 | 5.3 | 14.7 | 0.3 | 4.2 | 0.4 | 2.9 | 19.4 | 0.3 | 0.1 | 0.1 | 7.2 | 1.3 | 0 |
| 0.35 | 48.2 | 7.7 | 0.6 | 3.3 | 1.2 | 3.3 | 0.1 | 25.3 | 0 | 2.1 | 6.2 | 0.1 | 0 | 0 | 2 | 0 | 0.1 |
| 0.14 | 53.6 | 12.1 | 0 | 1.8 | 0.7 | 3.3 | 0 | 17.8 | 0 | 1.9 | 7.9 | 0 | 0 | 0 | 0.7 | 0 | 0.2 |
| 0.08 | 65.4 | 11.5 | 0 | 1.2 | 0.3 | 1.2 | 0 | 14.5 | 0 | 2.0 | 3.4 | 0 | 0 | 0 | 0.4 | 0 | 0 |

## c. Vertical distribution of aerosol properties by lidar measurements

Lidars are the main devices to retrieve vertical-resolved aerosol optical properties during both day- and nighttime. Lidar measurements only performed on 30 June are shown in Figs. 7 and 8. In particular, Fig. 7 shows the daily evolution of aerosol backscatter coefficient profiles retrieved from lidar measurements performed at different daytime hours between 1615 and 2326 UTC. Error bars indicate one standard deviation caused by statistical uncertainties and have been calculated from the law of error propagation by assuming a Poisson noise on lidar signals (De Tomasi et al. 2003). Aerosol backscatter coefficient profiles of Figs. 7a–d have been retrieved by using the Klett inversion technique (Fernald 1984). The reference height $z_o$ representing the height at which the aerosol backscatter coefficient $\beta(z_o) = 0$ has been located at an altitude between 8 and 10 km. These clear-air conditions normally prevail in the upper troposphere. The Klett inversion technique also requires a hypothesis on the extinction-to-backscatter coefficient ratio (lidar ratio). The lidar ratio depends on size distribution, shape, and chemical composition of the particles and, as a consequence, it allows for the characterization of aerosols of different origins and types (e.g., Sasano and Browell 1989; Ackermann 1998; Matthias and Bösenberg 2002). We have set the lidar ratio equal to 53 sr to retrieve the aerosol backscatter coefficient profiles plotted in Figs. 7a–d. This choice will be explained later. The aerosol backscatter coefficient profiles of Figs. 7e,f have been retrieved by the Raman lidar technique (Ansmann et al. 1992). Figure 7 shows that the aerosol layer extending up to ~5.5 km is rather uniform at least from 1630 to 1950 UTC. Total depolarization ratio vertical profiles (Fig. 7, gray lines) that have been performed only on the early afternoon of 30 June, support the last comment. The total depolarization ratio, being the ratio between the total depolarized backscatter coefficient and the total polarization preserving backscatter coefficient, has a value of 0.014 in a pure molecular atmo-

sphere and generally higher values in presence of aerosols. The total depolarization ratio is affected by the aerosol morphology: spherical particles produce a low depolarization, while depolarization ratios larger than 10%–15% are associated to nonspherical particles, such as desert dust particles (e.g., Müller et al. 2003; Tafuro et al. 2006). Therefore, as a consequence of the advection of nonspherical dust particles, we observe from Fig. 7a that the total depolarization ratio is ~10% from 2 to 8 km. According to sun/sky radiometer measurements, the dust event intensity decreases with the time of the day on 30 June and, as a consequence, total depolarization ratio values of Fig. 7b are smaller than those of Fig. 7a. In addition, Fig. 7f shows that the altitude at which aerosols are detected by the lidar decreases up to 4 km at midnight. AOTs at 351 nm retrieved from lidar measurements are plotted in Fig. 5 (full dots). Uncertainties on lidar AOT values are lower than 2%. Lidar AOT values are in satisfactory accordance with those obtained by sun/sky radiometer measurements and show that the dust event intensity decreases at night on 30 June.

Figure 8 shows the vertical profiles of the aerosol extinction coefficient and of the lidar ratio retrieved by Raman lidar measurements performed from 2057 to 2326 UTC. Our lidar system allows Raman lidar measurements only at nighttime. The extinction profile is calculated by a linear fit of the logarithm of the Raman signal (e.g., De Tomasi et al. 2003), and error bars are one standard deviation in the slope of the fitting straight line. According to past studies (e.g., Barnaba et al. 2004), the high lidar ratio values in Fig. 8 (gray symbols) can be due to the presence of nonspherical dust particles. Figure 8 shows that lidar ratio values do not vary with altitude, at least within error bars. Lidar ratios depend on size distribution, shape, and chemical composition of particles. Thus, the lidar ratio plots in Fig. 8 are consistent with the hypothesis that the aerosol layer detected by the lidar was made of particles with rather similar optical and microphysical properties. In addition, total depolarization ratio profiles indicate that
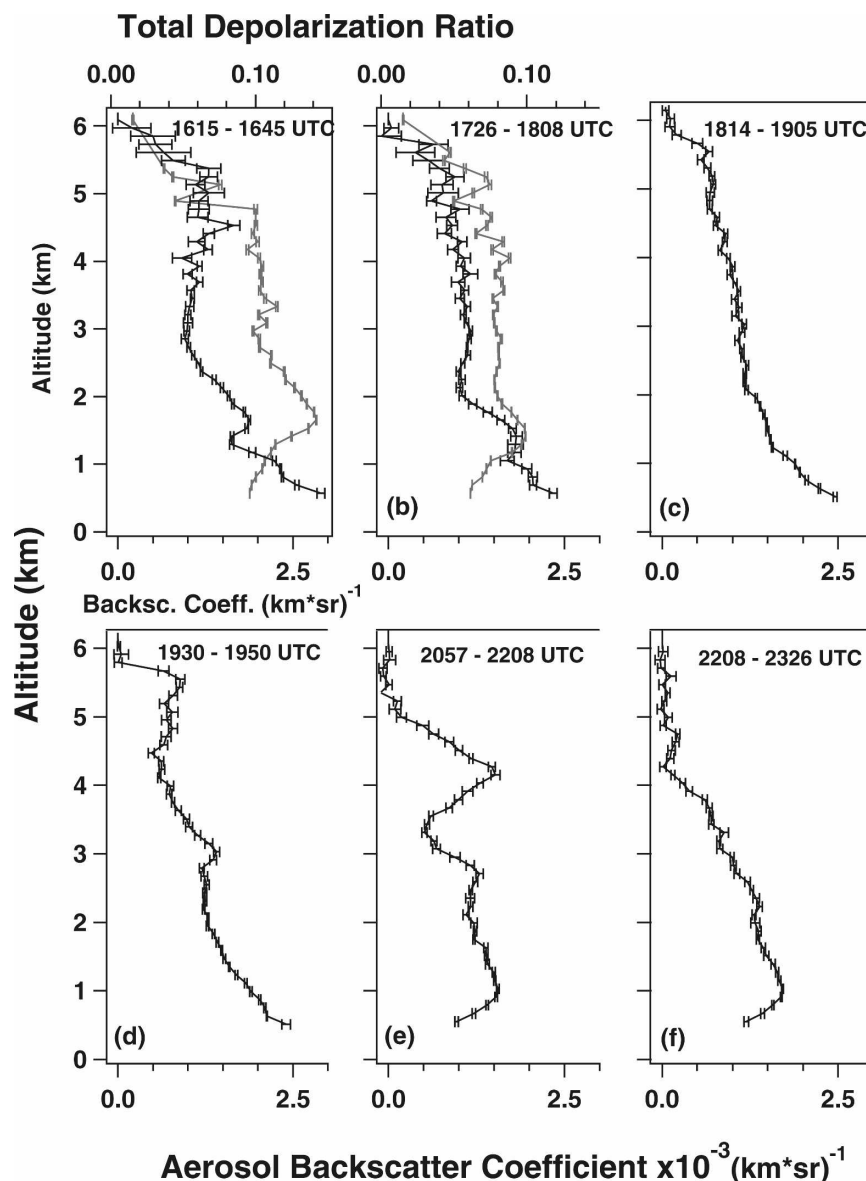
FIG. 7. Aerosol backscatter coefficient vertical profiles retrieved on 30 Jun 2005 from lidar measurements at different daytime hours. Gray dotted lines provide total depolarization ratio vertical profiles.

the aerosol particle morphology was rather uniform within the layer. These last observations are consistent with the hypothesis that ground-collected particles were quite representative of those located above the ground level. The fractional collection of particles by the seven-stage cascade impactor, which has provided a mass distribution well correlated to the mean sun/sky radiometer volume size distribution of Fig. 4, supports the last comment.

Finally, it is worth mentioning that we have assumed that the aerosol layer monitored by the lidar during the daytime hours was characterized by a lidar ratio value equal to the mean lidar ratio value retrieved from the nighttime Raman lidar measurements, which is equal to 53 sr. The latter assumption is also supported by sun/sky radiometer measurements performed on 30 June, as outlined below. The column-averaged lidar ratio ($S$) at a given wavelength $\lambda$ from sun/sky radiometer measurements can be calculated according to the following equation (Müller et al. 2003):

$$S(\lambda) = \frac{4\pi}{\text{SSA}(\lambda)P(\lambda, 180°)}, \qquad (1)$$
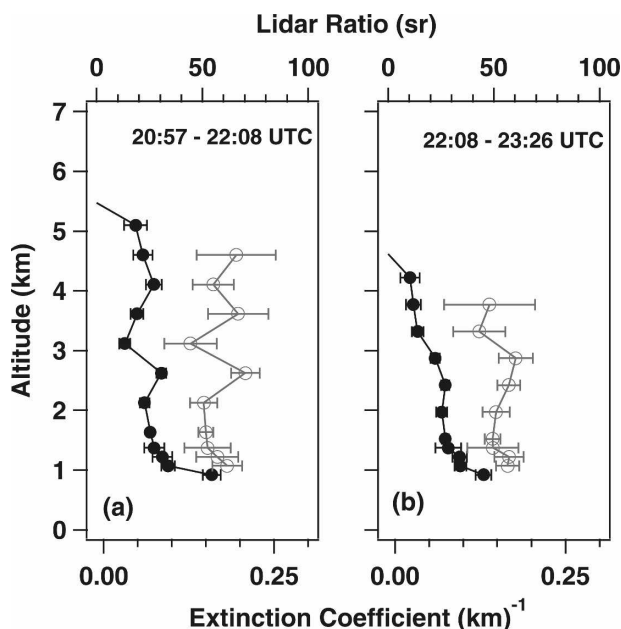
FIG. 8. Vertical profiles of the aerosol extinction coefficient (black symbols) and of the lidar ratio (gray symbols) retrieved on 30 Jun 2005 from nighttime Raman lidar measurements.

where $P(\lambda, 180°)$ is the particle phase function value at 180°. According to SSA and phase function values at $\lambda = 440$ nm retrieved from the spheroid almucantar retrieval model on 30 June at different daytime hours, the mean column-averaged lidar ratio is $S$ (440 nm) = 49 ± 11. The latter value is in satisfactory accordance to the mean lidar ratio value from lidar measurements.

### d. Aerosol characterization by SEM and EDX microanalysis

The seven-stage impactor filters have been examined by a field-emission scanning electron microscope SEM (JEOL, model JSM-6480LV), equipped with an energy dispersive X-ray (EDX) system (model EDS 2000), to characterize morphological properties of the collected particles and perform a semiquantitative analysis of their elemental composition. The system allows analysis of elements having an atomic number ≥5. Operating conditions for SEM analysis were as follows: accelerating voltage: 20 kV; probe current: 75 $\mu$Å; working distance: 10 mm; accumulation time: 30 s for EDX spectra and 1800 s for marked images; and dead time: 25%–30%. SEM images of randomly chosen areas at magnifications of 2000 have mainly been used to test the impactor fractional sampling, to analyze morphology and elemental composition of single particles, and to infer their chemical composition. It is worth mentioning that EDX spectra do not allow inferring chemical species

without ambiguity. However, we believe that it is possible to infer the presence of some chemical species when the chemical composition of particles is simple (Perrone et al. 2006).

Figures 9a,b show SEM images of the particles collected on randomly selected areas of the impactor filter with $d_c = 2.7$ $\mu$m and $d_c = 0.35$ $\mu$m, respectively. Besides the quartz filter fibers, Fig. 9a shows that the shape of the collected particles, often clustered together, is quite irregular. Single particles cannot even be detected in Fig. 9b. Magnifications much larger than 2000 would have been required since their size is rather small and their number is rather large. According to the mean volume size distribution profile retrieved by the sun/sky radiometer measurements and shown in Fig. 4 (gray symbol), the number of atmospheric particles with 0.35-$\mu$m diameter is more than 100 times larger than that of particles with 2.7-$\mu$m diameter.

SEM–EDX analyses on the particles in Fig. 9a have revealed the presence of particles containing two or more of the following elements: C, N, F, Na, Mg, Al, P, S, Cl, K, Ca, Ti, Fe, and Zn. Even though Si and O have been detected, they have not been considered in the data analysis because they are major components of quartz filters. Selected elements (i.e., C, Na, Mg, Al, Cl, K, Ca, and Fe) have been marked on the SEM image in Fig. 9a and the corresponding images are shown in Figs. 10a–h. This method allows getting the spatial distribution of the selected elements in the sample and in single particles and can allow us to infer the chemical composition of particles and retrieve some information on particle morphology. We observe from Fig. 10 that Na (Fig. 10a) and Cl (Fig. 10b) have a rather similar spatial distribution on the selected filter area and, as a consequence, the marked images allow us to infer the presence, location, and size of NaCl particles. The comparison of the marked areas in Figs. 10c–f, allows us to infer the presence of single particles or clustered particles made of elements typical of illite/smectite (e.g., Al, K, Fe, and Mg). SEM-marked images have also allowed us to infer the presence of elements typical of dolomite (e.g., Ca, Mg, and C), and carbonate (e.g., Ca and C) particles. Illite/smectite and dolomite are the major components of dust coming from northwestern Africa (e.g., Avila et al. 1997; Blanco et al. 2003). The element-marked images in Fig. 9b have instead allowed us to infer the presence of particles with a large content of C, S, N, and to a less extent of Ca and Na. Single particle EDX spectra at larger magnifications have also been used to further support the above comments on the chemical composition of particles. EDX analyses have been performed on many randomly selected areas to get the mean elemental composition of the particles
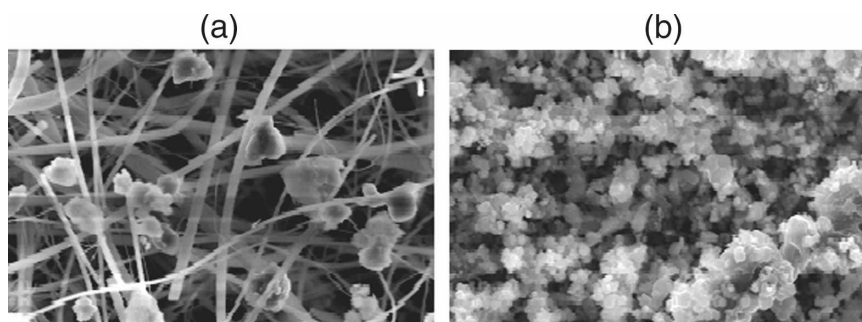
FIG. 9. SEM images of the particles collected on randomly chosen areas of the impactor filters with 50% effective-cut diameter of (a) 2.7 and (b) 0.35 $\mu$m.

collected on each filter. In particular, the intensities of EDX spectrum lines have been converted to corresponding percents of weight concentrations by a standardless ZAF (atomic number Z, absorption, and fluorescence) correction method in which ideal flat samples have been assumed (e.g., Paoletti et al. 2002) to get semiquantitative data on weight concentrations (%) of some selected elements (e.g., C, N, F, Na, Mg, Al, P, S, Cl, K, Ca, Ti, V, Mn, Fe, Cu, and Zn). The results

referring to the seven impactor filters are shown in Fig. 11 and Table 2. According to Figs. 9 and 10, Fig. 11 shows that both size and mean particle composition vary with $d_c$: sea salt and particles of crustal origin mainly affect the mass composition of the impactor filters with $d_c \geq 0.65$ $\mu$m, even if the contribution of Ca decreases and that of S increases as $d_c$ varies from 5.7 to 0.65 $\mu$m. In addition, Fig. 11 clearly shows that the mean particle composition of filters with $d_c \leq 0.35$ $\mu$m
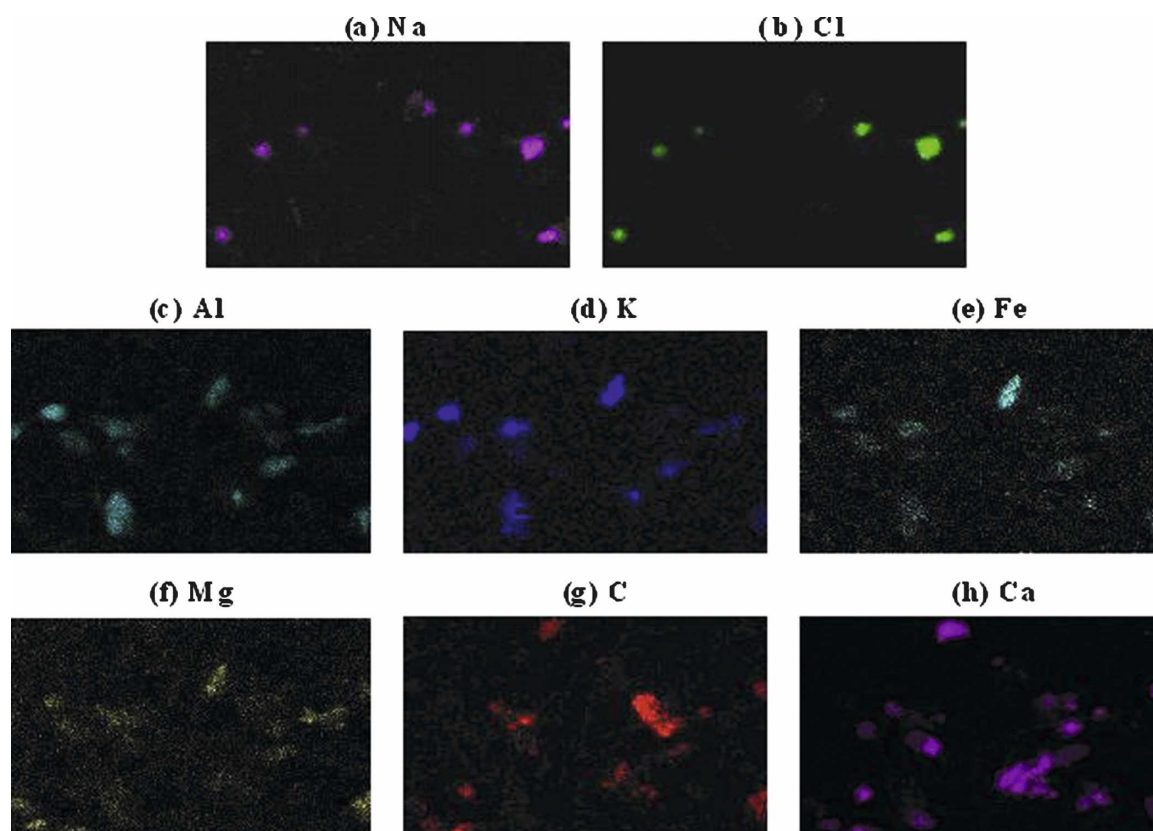


FIG. 10. Selected elements (i.e., C, Na, Mg, Al, Cl, K, Ca, and Fe) marked on the SEM image in Fig. 9a.
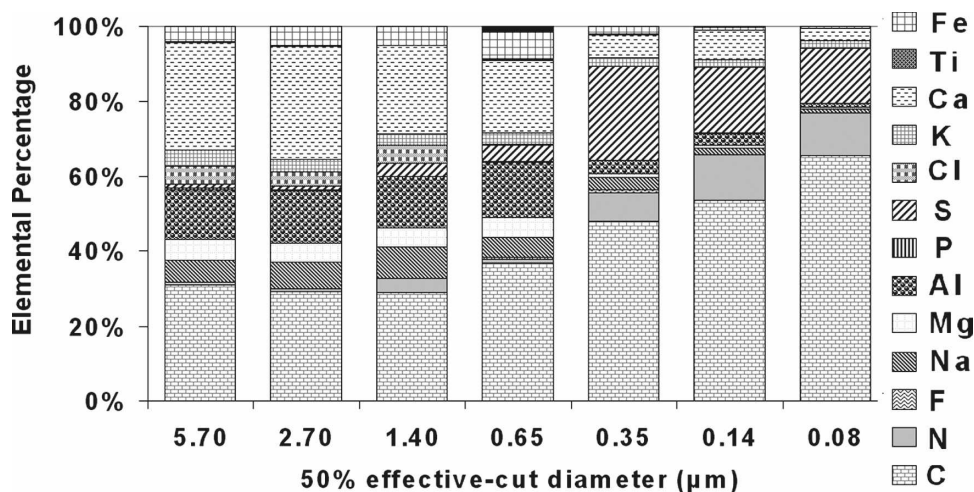
FIG. 11. Elemental weight concentrations (%) in the analyzed impactor filters.

is significantly different than that of filters with $d_c \geq$ 0.65 $\mu$m: the sulfur and nitrogen weight percentage is 33% on the filter with $d_c = 0.35$ $\mu$m, while it is 5% on the $d_c = 0.65$ $\mu$m filter. The aluminum weight percentage is 3% on the filter with $d_c = 0.35$ $\mu$m, while it is 15% on the $d_c = 0.65$ $\mu$m filter, and of about 14% on the filters with $d_c > 0.65$ $\mu$m. The mean columnar volume size distribution in Fig. 4 (gray symbols) retrieved from sun/sky radiometer measurements performed during the impactor measurement time reveals that fine- and coarse-mode modal radius are at ~0.06 and ~1.5 $\mu$m, respectively. Hence, we believe that SEM analyses on the impactor filters with $d_c \geq 0.65$ $\mu$m and with $d_c \leq$ 0.35 $\mu$m allow getting some information on the elemental composition of coarse- and fine-mode atmospheric particles, respectively.

### e. Ion chromatography analyses on the PM2.5 sample: Methodology and results

A high-performance ion chromatograph DIONEX DX-500 has been used to determine the mass concentration of the major anions (i.e., $Cl^-$, $NO_3^-$, $SO_4^{2-}$, and $F^-$) and cations (i.e., $Na^+$, $NH_4^+$, $K^+$, $Mg^{2+}$, and $Ca^{2+}$) on the 24-h PM2.5 sample collected on 30 June. In particular, a self-regenerating suppressor ASRS-ULTRA (4 mm) at 50 mA, a guard column IONPAC AG4A-SC (4 × 50 mm) and an analytical column IONPAC AS4A-SC (4 × 250 mm) were used for anion analyses.

All the anions were determined with isocratic elution at 2.0 mL min$^{-1}$ of 1.8 mM $Na_2CO_3$/1.7 mM $NaHCO_3$ eluent. For cations analysis we used a self-regenerating suppressor CSRS-ULTRA (4 mm), a guard column IONPAC CG12A (4 × 50 mm) at 100 mA, and an analytical column IONPAC CS12A (4 × 250 mm). All the cations were determined with isocratic elution at 1 mL min$^{-1}$ of 20 mN $H_2SO_4$ eluent.

Ion mass concentrations are given in Table 3. We observe that the mass concentration of the tested ions is 36% of the total PM2.5 mass concentration. Mass percentages of tested ions are also shown in Fig. 12. We observe from Table 2 and Fig. 12 that $NO_3^-$, $SO_4^{2-}$, and $Ca^{2+}$ are the main ion components: their mass represents 89% of the total ion mass. In addition, we note that $SO_4^{2-}$ is the main ion component of fine-mode particles, in accordance to previous studies (Kouyoumdjian and Saliba 2005) and that its level (6.4 $\mu$g m$^{-3}$) is comparables to the $SO_4^{2-}$ levels reported for coastal sites of the central-eastern Mediterranean (e.g., Bardouki et al. 2003). The latter results show the significant contribution of sulfates and nitrates to the fine fraction of the aerosol load even during a dust event in accordance to SEM analyses on impactor filters (Fig. 11). We believe that the rather high mass concentrations of $K^+$, $Mg^{2+}$, and $Ca^{2+}$ reported in Table 3, are due to the Saharan dust particles collected on 30 June, being $K^+$, $Mg^{2+}$, and $Ca^{2+}$ elements of illite/smectite and dolo-

TABLE 3. Mass concentrations ($\mu$g m$^{-3}$) of the investigated ion species in the 24-h PM2.5 sample collected on 30 Jun.

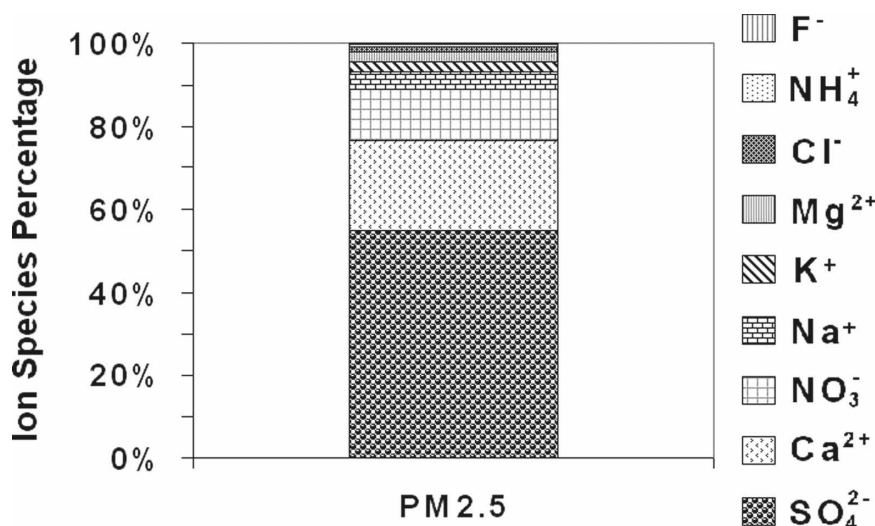| Date | $Na^+$ | $NH_4^+$ | $K^+$ | $Mg^{2+}$ | $Ca^{2+}$ | $F^-$ | $Cl^-$ | $NO_3^-$ | $SO_4^{2-}$ | PM2.5 | Ions/PM2.5 | Cation deficit ($\mu$equ m$^{-3}$) |
|---|---|---|---|---|---|---|---|---|---|---|---|---|
| 30 Jun 2005 | 0.5 | 0.5 | 0.3 | 0.3 | 2.5 | 0.4 | 0.2 | 1.4 | 6.4 | 33 | 36% | 2.6 |

FIG. 12. Ion species mass percentage (%) in the 24-h PM2.5 sample collected on 30 Jun.

mite particles. In fact, Kouyoumdjian and Saliba (2005) have found in PM2.5 samples collected over the eastern Mediterranean, annual mean concentrations of 0.08, 0.03, and 0.52 $\mu$g m$^{-3}$ for K$^+$, Mg$^{2+}$, and Ca$^{2+}$, respectively. In contrast, we have found mass concentrations of 0.29, 0.28, and 2.5 $\mu$g m$^{-3}$ for K$^+$, Mg$^{2+}$, and Ca$^{2+}$, respectively. Finally, the ion balance revealed a cation deficit of 2.6 $\mu$equ m$^{-3}$. The cation deficit, which is defined as an excess of negative charge, is given by the sum of anions minus the sum of cations, expressed in equivalents. According to Mihalopoulos et al. (1997), high cation deficit values are due to the presence of air masses affected by anthropogenic pollution and generally transported over the Mediterranean from western or northern Europe.

## 4. Estimation of the aerosol mass loading on 30 June 2005

The lidar and sun/sky radiometer measurements collocated in time and space, and data on the elemental composition of ground-measured fine- and coarse-mode particles are used in this section to retrieve vertical profiles of particle number and mass concentrations due to fine- and coarse-mode particles.

It is well known (e.g., Wandinger 2005) that the aerosol backscatter coefficient $\beta(z, \lambda)$ is the primary atmospheric parameter that determines the strength of the lidar signal. It describes the fraction of laser light scattered by aerosol particles into the backward direction (i.e., toward the lidar receiver). According to Mie's theory, for a laser light of wavelength $\lambda$ and at a distance $z$ from ground, the aerosol backscatter coefficient can be written as

$$\beta(z, \lambda) = \sum_i N_i(z) \frac{d\sigma_{i,\text{scat}}(\lambda, 180°)}{d\Omega}, \qquad (2)$$

where $N_i$ is the number concentration of scattering particles of kind $i$ in the volume illuminated by the lidar laser pulse and $d\sigma_{i,\text{scat}}(\lambda)/d\Omega$ is the particle differential scattering cross section at the laser wavelength and for the backward direction (Bohren and Huffman 1983). Following Eq. (2), we can determine the vertical distribution of the number concentration of scattering particles $N_i$ by using the aerosol backscatter coefficient vertical profile retrieved by lidar measurements at $\lambda = 351$ nm and by calculating the $d\sigma_{i,\text{scat}}(\lambda, 180°)/d\Omega$ for spherical scattering particles of kind $i$. Sun/sky radiometer measurements have been used in this study to retrieve the particle microphysical parameters that are required to calculate the particle differential scattering cross section. In particular, the backscatter coefficient vertical profile in Fig. 7a that has been retrieved on 30 June by lidar measurements performed from 1615 to 1645 UTC and the sun/sky radiometer measurements performed at 1626 UTC have been used to calculate the backward-direction differential scattering cross section and to retrieve the vertical profile of $N_i(z)$. Figures 13a,b show the columnar volume ($dV/d\ln r$) and particle size distribution ($dN/d\ln r$), respectively, retrieved on 30 June from sun/sky radiometer measurements performed at 1626 UTC. Both curves have been fitted by a bimodal lognormal distribution with the number distribution fine- and coarse-mode modal radius at 0.07 and 0.62 $\mu$m, respectively. The corresponding normalized bimodal lognormal function has then been used to calculate the backward-direction differential scattering cross section for the fine- and coarse-mode scattering
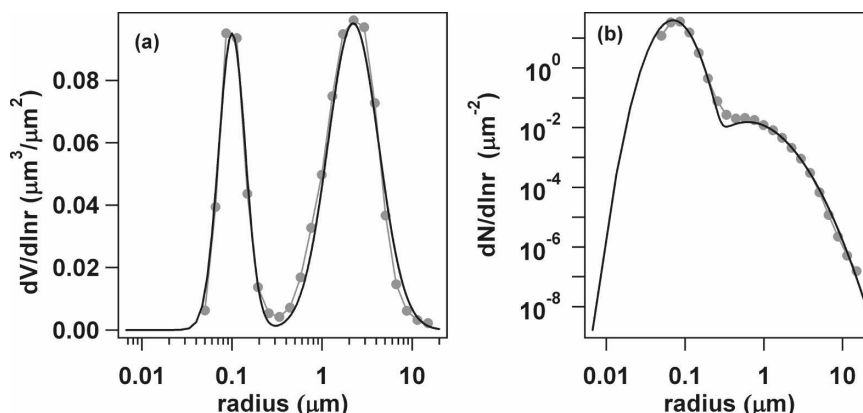
FIG. 13. (a) Columnar volume and (b) particle size distribution retrieved on 30 Jun 2005 from sun/sky radiometer measurements at 1626 UTC (symbols). Solid lines represent bimodal lognormal fitting curves.

particles. In addition, we assumed that the columnar real (1.33 ± 0.04) and imaginary (0.003 ± 0.001) refractive index at 440 nm, retrieved on 30 June from sun/sky radiometer measurements at 1626 UTC, could be ascribed to both the fine- and the coarse-mode particles and could also be used at the laser wavelength of 351 nm. According to d'Almeida et al. (1991), the latter condition is not very restrictive. Finally, we have assumed that refractive index values and normalized particle size distribution were independent of the altitude $z$; this is a quite restrictive assumption. However, we believe that experimental data from lidar, sun/sky radiometer, and in situ measurements performed during the dust event analyzed in this paper support the latter assumption. Both the aerosol backscatter coefficient and the total depolarization ratio vertical profiles in Fig. 7a, indicate that the aerosol particles were well mixed within the layer detected by the lidar. The satisfactory accordance on 30 June, between the mean column-averaged lidar ratio value from diurnal sun/sky radiometer measurements and the nighttime lidar ratio profile (Fig. 8b, gray line) further support the assumption. The vertical profile of the total number concentration of scattering particles ($N$) calculated in accordance to the above-mentioned assumptions is plotted in Fig. 14. Error bars represent uncertainties only due to $\beta(z)$ uncertainties. We observe that $N$ varies with altitude within the $(3–10) \times 10^9$ m$^{-3}$ range. In addition, it is worth noting that 30% changes of the imaginary refractive index value affect the number concentration of scattering particles less than 1%, while 3% changes of the real refractive index value may affect $N$ values up to 10%.

According to the elemental composition of particles collected on impactor filters (section 3d) and ion chromatography analyses of the PM2.5 sample collected on 30 June (section 3e), fine-mode particles, mainly of anthropogenic origin, were made of sulfates, nitrates, and carbon, while coarse-mode particles were mainly of crustal and marine origin. Following d'Almeida et al.
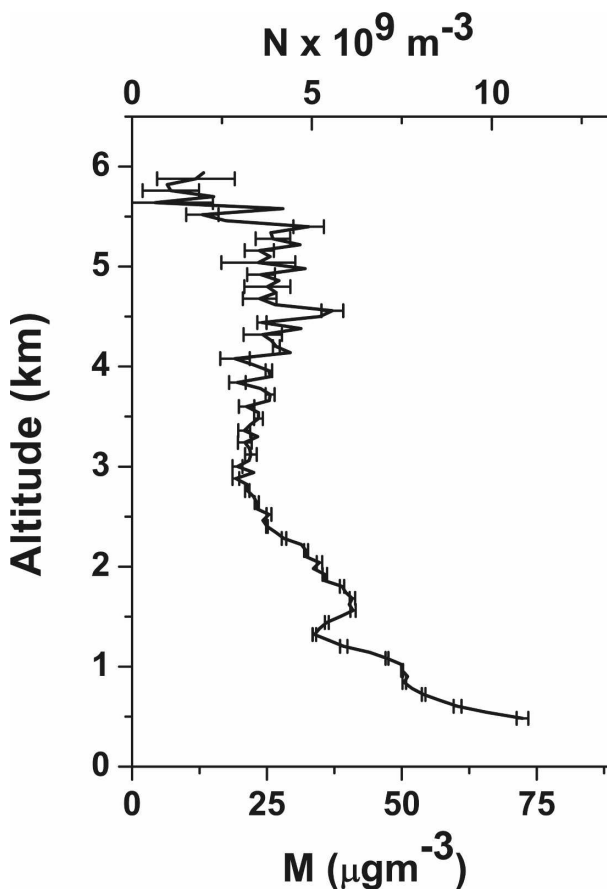


FIG. 14. Vertical profile of the calculated mass and number concentration of scattering particles.

(1991) we have assumed that the mass density of fine- and coarse-mode particles was 2 and 2.5 $\mu$g m$^{-3}$, respectively. The calculated mass concentration ($M$) vertical profile is also plotted in Fig. 14, and it is worth noting that 52% of the total mass concentration is due to fine-mode particles, while 48% is due to coarse-mode particles. By changing of 20% fine- or coarse-mode particle mass-density values, mass concentrations vary ~10%. We observe in Fig. 14 that the mass concentration due to all particles is $M = 72$ $\mu$g m$^{-3}$ at 480 m above ground level. The latter result is in satisfactory accordance with the TSP mass concentration (69 $\pm$ 3 $\mu$g m$^{-3}$) monitored at the ground on 30 June at about 1630 UTC (Fig. 3b, solid line), if we assume that particle number concentration and hence mass concentration do not significantly vary with altitude within the PBL height that was about 470 m (Fig. 3c, black line). The PBL height is the height of the well-mixed layer closest to the ground level (Coulter 1979). In addition, it is also worth noting that the 24-h TSP and PM2.5 samplings performed on 30 June have revealed that the PM2.5 mass concentration was 60% of the TSP mass concentration. The latter result is also in satisfactory accordance with the fine fraction mass concentration (52%) above retrieved, by noting from Fig. 13a that the maximum radius of fine-mode particles is smaller than 1.25 $\mu$m.

We believe that the results of the study reported in this section, although based on some a priori assumptions, represent an example on the potential capabilities of complementary measurements by passive and active remote sensing techniques, and in situ observations, to retrieve with satisfactory confidence, data on the vertical distribution, concentration, composition, dimension, and optical properties of aerosol particles. All these parameters are of particular importance to properly estimate the radiative forcing due to troposphere aerosols. The uniform distribution of aerosol particles with altitude is the strongest assumption in the methodology suggested in this last section. Lidar profiles have been used to support this assumption during the dust outbreak analyzed in the paper. Nevertheless, we have found that ground-based in situ measurements and sun/sky radiometer measurements further support lidar measurements.

## 5. Summary and conclusions

Ground-based in situ measurements and remote sensing observations by a Raman lidar and a sun/sky radiometer have been performed to characterize the aerosol load temporal evolution, main composition, optical, and microphysical properties of aerosol particles

from 29 June to 1 July 2005. According to MODIS true color images and analytical back trajectories, the central-eastern Mediterranean Basin and, hence the monitoring site, have been affected by the advection of dust particles from the northwestern Sahara on those days. Sun/sky radiometer measurements, besides highlighting changes of aerosol microphysical properties, have also allowed us to characterize the diurnal temporal evolution of the aerosol load from 29 June to 1 July. The AOT temporal evolution has indicated that a significant advection of dust particles over the monitoring site started to occur on the afternoon of 29 June. The latter results are also supported by the increase (decrease) of the mean ground temperature (relative humidity) and of the TSP mass concentration observed at the ground level. The advection of dust particles was also quite significant on 30 June: AOTs at 380 nm varying within the 0.43–0.48 range and TSP mass concentrations varying within the 45–80 $\mu$g m$^{-3}$ range have been observed during the daytime hours. Angstrom coefficient values that varied within the 0.7–0.6 range on 30 June and were both larger on 29 June and 1 July, revealed that the contribution of large dust particles was larger on 30 June. In fact, the comparison of the mean columnar particle size distribution of 30 June with those referring to 29 June and 1 July revealed that the contribution of coarse-mode particles was larger on 30 June. Raman lidar measurements performed on 30 June have allowed us to retrieve results on the evolution of the AOT at 351 nm up to the nighttime. In particular, backscatter coefficient vertical profiles have revealed that on the afternoon of 30 June the aerosol layer extending up to ~5.5 km was rather uniform and that the layer was located below 4 km at night (~2300 UTC). Total depolarization and lidar ratio vertical profiles have allowed us to infer that aerosol particles were well mixed within the aerosol layer. The latter results have allowed us to assume that the columnar size distribution retrieved by sun/sky radiometer measurements could be considered representative of the particle size distribution all along the aerosol layer. We believe that the satisfactory correlation between the columnar volume size distribution and the particle mass distribution on the seven-stage cascade impactor filters further supports the previous conclusion.

Ion chromatography analyses on the 24-h PM2.5 sample collected at ground on 30 June, besides providing the mass concentration of major anions (i.e., Cl$^-$, NO$_3^-$, and SO$_4^{2-}$) and cations (i.e., Na$^+$, NH$_4^+$, K$^+$, and Mg$^{2+}$), which was 36% of the total PM2.5 mass concentration, allowed us to infer that K$^+$, Mg$^{2+}$, and Ca$^{2+}$ ions were mainly due to the presence of dust particles: K, Mg, and Ca are main elements of illite/smectite and

dolomite, which are the major mineral components of particles coming from northwestern Africa. The quite significant mass concentration of $SO_4^{2-}$, $NO_3^-$, and $NH_4^+$ ions has instead been ascribed to anthropogenic pollution of local origin or advected over the monitoring site from northern and eastern Europe. Morphological and elemental analyses by SEM on the seven impactor filters revealed the significant dependence of particles' size, shape, and number on the 50% effective-cut diameter of the filters and have allowed us to infer that nitrates, sulfates, and carbon were the main aerosol components of fine-mode particles, while sea salts, carbonates, and minerals were the main aerosol components of coarse-mode particles. In particular, it has also been shown that dust particles mainly affect the coarse-mode aerosol and that the anthropogenic fine-mode aerosol can represent more than 50% of the aerosol load even during a dust outbreak.

Finally, the potential capabilities of complementary measurements by passive and active remote sensing techniques and ground-based in situ measurements to retrieve with satisfactory confidence the vertical distribution of the particle number and mass concentration have been analyzed and discussed.

In conclusion, the main goal of this paper was to present a Saharan dust event study that can be of interest for the Mediterranean climatology, where complementary measurements by a lidar and a sun/sky radiometer, ground observations, and chemical and morphological analyses have been properly combined to infer optical and microphysical aerosol properties and the atmospheric aerosol composition. The results presented in the paper clearly revealed how a dust event can affect meteorological parameters, chemical, and microphysical aerosol properties up to the ground level.

REFERENCES

Ackermann, J., 1998: The extinction-to-backscatter ratio of tropospheric aerosol: A numerical study. *J. Atmos. Oceanic Technol.,* **15,** 1043–1050.

Allegrini, I., A. Febo, A. Pasini, and S. Schiarini, 1994: Monitoring of the nocturnal mixed layer by means of particulate radon progeny measurement. *J. Geophys. Res.,* **99,** 18 765–18 777.

Ansmann, A., U. Wandinger, M. Riebesell, C. Weitkamp, E. Voss, W. Lahmann, and W. Michaelis, 1992: Combined Raman elastic-backscatter lidar for vertical profiling of moisture, aerosols extinction, backscatter, and lidar ratio. *Appl. Phys.,* **55B,** 18–28.

Avila, A., I. Queralt-Mitjans, and M. Alarc, 1997: Mineralogical composition of African dust delivered by red rains over the northeastern Spain. *J. Geophys. Res.,* **102,** 21 977–21 996.

Bardouki, H., and Coauthors, 2003: Chemical composition of size-resolved atmospheric aerosols in the eastern Mediterranean during summer and winter. *Atmos. Environ.,* **37,** 195–208.

Barnaba, F., F. de Tomasi, G. P. Gobbi, M. R. Perrone, and A. Tafuro, 2004: Extinction versus backscatter relationships for lidar applications at 351 nm: Maritime and desert aerosol simulations and comparison with observations. *Atmos. Res.,* **70,** 229–259.

Blanco, A., F. de Tomasi, E. Filippo, D. Manno, M. R. Perrone, A. Serra, A. M. Tafuro, and A. Tepore, 2003: Characterization of African dust over southern Italy. *Atmos. Chem. Phys.,* **3,** 1–13.

Bohren, C. F., and D. R. Huffman, 1983: *Absorption and Scattering of Light by Small Particles.* Wiley and Sons, 530 pp.

Buccolieri, A., G. Buccolieri, A. Dell'Atti, M. R. Perrone, and A. Turnone, 2006: Natural sources and heavy metals. *Ann. Chimica,* **96** (3–4), 167–181.

Coulter, R. L., 1979: A comparison of three methods for measuring mixing-layer height. *J. Appl. Meteor.,* **18,** 1496–1499.

d'Almeida, G. A., P. Koepke, and E. P. Shettle, 1991: *Atmospheric Aerosols—Global Climatology and Radiative Characteristics.* A. Deepak Publishing, 561 pp.

De Tomasi, F., and M. R. Perrone, 2003: Lidar measurements of tropospheric water vapor and aerosol profiles over southeastern Italy. *J. Geophys. Res.,* **108,** 4286, doi:10.1029/2002JD002781.

——, A. Blanco, and M. R. Perrone, 2003: Raman lidar monitoring of extinction and backscattering of Africa dust layers and dust characterization. *Appl. Opt.,* **42,** 1699–1709.

——, A. M. Tafuro, and M. R. Perrone, 2006: Height and seasonal dependence of aerosol optical properties over south-east Italy. *J. Geophys. Res.,* **111,** D10203, doi:10.1029/2005JD006779.

Di Iorio, T., A. di Sarra, W. Junkermann, M. Cacciani, G. Fiocco, and D. Fuà, 2003: Tropospheric aerosols in the Mediterranean: 1. Microphysical and optical properties. *J. Geophys. Res.,* **108,** 4316, doi:10.1029/2002JD002815.

Dubovik, O., and M. D. King, 2000: A flexible inversion algorithm for retrieval of aerosol optical properties from sun and sky radiance measurements. *J. Geophys. Res.,* **105,** 20 673–20 696.

——, A. Smirnov, B. N. Holben, M. D. King, Y. J. Kaufman, T. F. Eck, and I. Slutsker, 2000: Accuracy assessments of aerosol optical properties retrieved from Aerosol Robotic Network (AERONET) sun and sky radiance measurements. *J. Geophys. Res.,* **105** (D8), 9791–9806.

——, B. N. Holben, T. F. Eck, A. Smirnov, Y. J. Kaufman, M. D. King, D. Tanré, and I. Slutsker, 2002: Variability of absorption and optical properties of key aerosol types observed in worldwide locations. *J. Atmos. Sci.,* **59,** 590–608.

——, and Coauthors, 2006: Application of spheroid models to account for aerosol particle nonsphericity in remote sensing

of desert dust. *J. Geophys. Res.,* **111,** D11208, doi:10.1029/2005JD006619.

Eck, T. F., B. N. Holben, J. S. Reid, O. Dubovik, S. Kinne, A. Smirnov, N. T. O'Neill, and I. Slutsker, 1999: The wavelength dependence of the optical depth of biomass burning, urban and desert dust aerosols. *J. Geophys. Res.,* **104,** 31 333–31 350.

Fernald, F. G., 1984: Analysis of atmospheric Lidar observations: Some comments. *Appl. Opt.,* **23,** 652–653.

Formenti, P., and Coauthors, 2002: STAARTE-MED 1998 summer airborne measurements over Aegean Sea. 2. Aerosol scattering and absorption, and radiative calculations. *J. Geophys. Res.,* **107,** 4451, doi:10.1029/2001JD001536.

Holben, B. N., and Coauthors, 1998: AERONET—A federated instrument network and data archive for aerosol characterization—An overview. *Remote Sens. Environ.,* **66,** 1–16.

——, and Coauthors, 2001: An emerging ground-based aerosol climatology: Aerosol optical depth from AERONET. *J. Geophys. Res.,* **106,** 12 067–12 097.

Kaufman, Y. J., D. Tanré, and O. Boucher, 2002: A satellite view of aerosols in the climate system. *Nature,* **419,** 215–223.

Klein, F., C. Randy, and L. Sowa, 1984: A new examination of the validity of the principle of beta radiation absorption for determination of ambient air dust concentration. *J. Aerosol Sci.,* **15,** 391–395.

Kouyoumdjian, H., and N. A. Saliba, 2005: Ion concentrations of PM10-2.5 and PM2.5 aerosols over the eastern Mediterranean region: Seasonal variation and source identification. *Atmos. Chem. Phys. Discuss.,* **5,** 13 053–13 073.

Matthias, V., and J. Bösenberg, 2002: Aerosol climatology for the plenary boundary layer derived from regular lidar measurements. *Atmos. Res.,* **63,** 221–245.

——, and Coauthors, 2004a: Vertical aerosol distribution over Europe: Statistical analysis of Raman lidar data from 10 European Aerosol Research Lidar Network (EARLINET) stations. *J. Geophys. Res.,* **109,** D18201, doi:10.1029/2004JD004638.

——, and Coauthors, 2004b: Aerosol lidar intercomparison in the framework of the EARLINET project: 1. *Instrument. Appl. Opt.,* **43,** 961–976.

Mihalopoulos, N., E. Stephanou, M. Kanakidou, S. Pilitsidis, and P. Bousquet, 1997: Troposheric aerosol ionic composition in the Eastern Mediterranean region. *Tellus,* **49B,** 314–326.

Müller, D., I. Mattis, U. Wandinger, A. Ansmann, D. Althausen, O. Dubovik, S. Eckhardt, and A. Stohl, 2003: Saharan dust over a central European EARLINET-AERONET site: Combined observations with Raman lidar and Sun photometer. *J. Geophys. Res.,* **108,** 4345, doi:10.1029/2002JD002918.

Paoletti, L., B. De Berardis, and M. Diociaiuti, 2002: Physicochemical characterisation of the inhalable particulate matter (PM10) in an urban area: An analysis of the seasonal trend. *Sci. Total Environ.,* **292,** 265–275.

Perrone, M. R., M. Santese, A. M. Tafuro, B. Holben, and A. Smirnov, 2005: Aerosol load characterization over South-East Italy by one year of AERONET sun-photometer measurements. *Atmos. Res.,* **75,** 111–133.

——, A. Turnone, A. Buccolieri, and G. Buccolieri, 2006: Particulate matter characterization at a coastal site in south-eastern Italy. *J. Environ. Monit.,* **8,** 183–190.

Robles Gonzalez, C., M. Schaap, G. de Leeuw, P. J. H. Builjes, and M. van Loon, 2003: Spatial variation of aerosol properties over Europe derived from satellite observations and comparison with model calculations. *Atmos. Chem. Phys.,* **3,** 521–533.

Sasano, Y., and E. V. Browell, 1989: Light scattering characteristics of various aerosol types derived from multiple wavelength lidar observations. *Appl. Opt.,* **28,** 1670–1679.

Schwartz, S. E., and M. O. Andreae, 1996: Uncertainty in climate change caused by anthropogenic aerosols. *Science,* **272,** 1121–1122.

Smirnov, A., B. N. Holben, T. F. Eck, O. Dubovik, and I. Slutsker, 2000: Cloud screening and quality control algorithms for aerosol data base. *Remote Sens. Environ.,* **73,** 337–349.

Tafuro, A. M., F. Barnaba, F. De Tomasi, M. R. Perrone, and G. P. Gobbi, 2006: Saharan dust properties over the central Mediterranean. *J. Atmos. Res.,* **81,** 67–93.

Tegen, I., P. Hollrigl, M. Chin, I. Fung, D. Jacob, and J. E. Penner, 1997: Contribution of different aerosol species to the global aerosol extinction optical thickness: Estimates from model results. *J. Geophys. Res.,* **102,** 23 895–23 915.

Wandinger, U., 2005: Introduction to Lidar. *LIDAR, Range-Resolved Optical Remote Sensing of the Atmosphere,* C. Weitkamp, Ed., Springer, 1–18.